Icarus 302 (2018) 109–125

Contents lists available at ScienceDirect

Icarus

journal homepage: www.elsevier.com/locate/icarus

Influence of petrographic textures on the shapes of impact experiment fine fragments measuring several tens of microns: Comparison with Itokawa regolith particles

Tatsuhiro Michikami[a,*], Tokiyuki Kadokawa[b], Akira Tsuchiyama[b], Axel Hagermann[c], Tsukasa Nakano[d], Kentaro Uesugi[e], Sunao Hasegawa[f]

[a] Faculty of Engineering, Kindai University, Hiroshima Campus, 1 Takaya Umenobe, Higashi-Hiroshima, Hiroshima 739-2116, Japan
[b] Division of Earth and Planetary Sciences, Graduate School of Science, Kyoto University, Kiashirakawao Iwake-cho, Sakyo-ku, Kyoto 606-8052, Japan
[c] School of Physical Sciences, The Open University, Walton Hall, Milton Keynes MK7 6AA, United Kingdom
[d] Geological Survey of Japan, National Institute of Advanced, Industrial Science and Technology, Tsukuba, 305-8568, Japan
[e] Japan Synchrotron Radiation Research, Institute (JASRI)/SPring-8, Sayo, Hyogo, 679-5198, Japan
[f] Institute of Space and Astronautical Science, Japan Aerospace Exploration Agency, Sagamihara, Kanagawa 252-8510, Japan

ARTICLE INFO

Article history:
Received 6 June 2017
Revised 30 September 2017
Accepted 30 October 2017
Available online 10 November 2017

Keywords:
Impact processes
Collisional physics
Asteroid Itokawa
Regoliths

ABSTRACT

In 2010, fine regolith particles on asteroid Itokawa were recovered by the Hayabusa mission. The three-dimensional microstructure of 48 Itokawa particles smaller than 120 μm was examined in previous studies. The shape distribution of Itokawa particles is distributed around the mean values of the axial ratio 2:$\sqrt{2}$:1, which is similar to laboratory impact fragments larger than several mm created in catastrophic disruptions. Thus, the Itokawa particles are considered to be impact fragments on the asteroid's surface. However, there have never been any laboratory impact experiments investigating the shapes of fine fragments smaller than 120 μm, and little is known about the relation between the shapes of fine fragments and the petrographic textures within those fragments. In this study, in order to investigate the relation between the petrographic textures and the shapes of fine fragments by impacts, the shapes of 2163 fine fragments smaller than 120 μm are examined by synchrotron radiation-based microtomography at SPring-8. Most samples are fine fragments from basalt targets, obtained in previous laboratory impact experiments by Michikami et al. (2016). Moreover, two impacts into L5 chondrite targets were carried out and the shapes of their fine fragments are examined for comparison. The results show that the shape distributions of fine fragments in basalt targets are similar regardless of impact energy per target mass (in contract to the shape distribution of relatively large fragments, which are affected by impact energy), and are similar to those in L5 chondrite targets and Itokawa regolith particles. The physical process producing these fine fragments would be due to multiple rarefaction waves in the target. Besides, the petrographic textures do not significantly affect the shapes of fine fragments in our experiments. On the other hand, according to Molaro et al. (2015), the shapes of the fragments produced by thermal fatigue by the day-night temperature cycles on the asteroid surface are influenced by the petrographic textures. Therefore, we conclude that the Itokawa particles are not the products of thermal fatigue but impact fragments on the asteroid surface.

1. Introduction

Since the pioneering work of Fujiwara et al. (1978), the shapes of fragments in laboratory impact experiments have often been characterized by axes *a*, *b* and *c*, these being the maximum dimensions of the fragment in three mutually orthogonal planes ($a \geq b \geq c$). In catastrophic disruption, the axial ratios of fragments are distributed around mean values of the axial ratios b/a ~0.7 and c/a ~0.5, i.e. corresponding to a:b:c in the simple proportion 2:$\sqrt{2}$:1 (Fujiwara et al., 1978; Capaccioni et al., 1984, 1986; Durda et al., 2015; Michikami et al., 2016). In impact cratering, on the other hand, the shapes of fragments are flatter, i.e. the mean axial ratios of b/a and c/a are ~0.7 and ~0.2, respectively (Michikami et al., 2016). Thus, the shapes of fragments in impact cratering are different from those in catastrophic disruption.

* Corresponding author.
E-mail address: michikami@hiro.kindai.ac.jp (T. Michikami).

https://doi.org/10.1016/j.icarus.2017.10.040

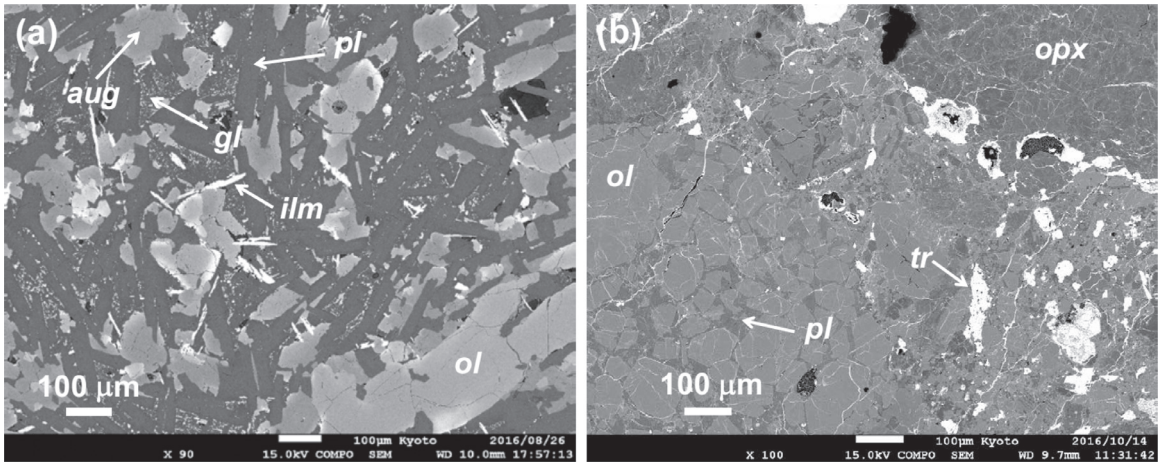

Fig. 1. Back-scattered electron images by a scanning electron microscope (JEOL JSM7001F) of the thin sections for the samples of the targets used. (a) Basalt sample (Linxi, Inner Mongolia). (b) L5 chondrite sample (Sayh al Uhaimir 001 meteorite, Oman). *ol*: olivine, *aug*: augite, *pl*: plagioclase, *ilm*: ilmenite, *gl*: mixture of glass and small mineral grains (mostly magnetite and ferroan augite), *opx*: orthopyroxene, and *tr*: troilite.

However, in laboratory impact experiments, only the shapes of fragments with sizes larger than several mm were investigated. In previous studies, there have only been very few laboratory impact experiments investigating the shapes of fragments with sizes less than 1 mm.

In 2010, regolith fine particles on asteroid Itokawa were recovered by the Hayabusa mission. Most of these sub-mm particles range from sub-micrometer to several tens of micrometers. Tsuchiyama et al. (2011, 2014) have examined the three-dimensional microstructure of 48 Itokawa regolith particles with sizes from 13.5 to 114.3 μm using synchrotron radiation (SR)-based microtomography at SPring-8 (they used the sphere-equivalent diameter, calculated from the particle volume, to define the size of these small particles). They suggested the Itokawa particles are fine fragments that originated primarily from impact phenomena. The Itokawa particles are consistent with LL chondrite material not only in terms of modal abundance as well as elemental and isotopic composition (Tsuchiyama et al., 2011; Nakamura et al., 2011; Yurimoto et al., 2011) of minerals but also in terms of their three-dimensional microstructure (Tsuchiyama et al., 2011). The shape distribution of the Itokawa particles (47 in total) is similar to fragments created laboratory experiments that resulted in catastrophic disruption of the target: their mean *b/a* and *c/a* ratios, calculated using the *EA* (*ellipsoidal approximation*) method (see Appendix A), are 0.72 and 0.44, respectively (Tsuchiyama et al., 2014). However, at less than 120 μm, the Itokawa particles measured using SR-based microtomography are significantly smaller than the relevant laboratory fragments, which were larger than several mm.

When comparing the Itokawa regolith particles with laboratory impact fragments or ordinary chondrites, we have to take into account (1) the effects of the mechanical process generating the fragments and (2) the petrographic characteristics of the particles themselves.

(1) Fragments of different shapes are affected in different ways by the mechanical process of the impact in that fragments are generally produced during the development of the rarefaction wave, which is the reflection of the shock wave on the target surface. For a given target size, relatively small fragments would be the products of a more complicated destruction as a result of multiple rarefaction waves in the targets (e.g., Fujiwara, 1980; Kadono and Arakawa, 2002). The multiple rarefaction waves in the targets would occur during catastrophic disruption. Therefore, it is necessary to investigate the relation between the degrees of destruction and the fine fragments.

(2) The shapes of very small fragments could be more dependent on petrographic characteristics than large fragment shapes. The size of the Itokawa particles is comparable to or less than the dimensions of petrographic textures and crystal grains, i.e. they are considerably smaller than the typical textural features of LL chondrites (e.g., a typical chondrule diameter is approximately 570 μm: Nelson and Rubin, 2002). It is necessary to investigate whether the petrographic textures and the crystal grain boundaries affect the shape of the Itokawa regolith particles because there might be a relationship between the two; for instance, Molaro et al. (2015) have shown that the grain distribution strongly influences the resulting size and shape of disaggregated material produced in thermal fatigue by the day-night temperature cycles on an asteroid.

In this study, most samples are fine fragments of basalt targets, obtained in previous laboratory impact experiments by Michikami et al. (2016). The shapes of these fine fragments, produced by impact events from cratering to catastrophic disruption, were systematically examined by SR-based microtomography. In order to investigate the relation between the petrographic textures and the shapes of fine fragments, the fine fragments in basalt targets were classified into three types: phenocryst-rich, groundmass-rich and intermediate. The shape distributions of each type were investigated. Moreover, two impacts into L5 chondrite targets were carried out for comparison. We used an L5 chondrite rather than LL5 or LL6 chondrites because it is difficult to obtain a large block of LL chondrites and the texture and mineralogy of these chondrites are not very different. Arguably, these represent better compositional analogues for the Itokawa regolith particles. The resulting shape distributions from basalt and L5 chondrite impacts are compared with that of the Itokawa particles. The research described here is intended to develop a deeper understanding of the formation of impact products and to constrain current interpretations of the origin of the Itokawa regolith particles.

2. Experimental method

2.1. Target properties

As mentioned above, we used basalt and L5 chondrite as target materials. Several samples of those target materials were reserved to investigate their petrographic textures and measure their

physical properties. Fig. 1 shows the scanning electron microscope (SEM) images of the thin sections for the samples of the target materials.

The sample from Linxi, Inner Mongolia is relatively coarse-grained basalt with very homogeneous texture on a scale of ~1 mm (Fig. 1a). The sizes of the phenocrysts composed of olivine and augite crystals are a few hundred micrometers. The lath-like crystals are plagioclase several tens of microns in length. Acicular (platy in 3D) crystals of ilmenite about 100 and 10 μm in length and width, respectively, are also present. The interstitial areas between these crystals are composed of a mixture of glass and fine mineral grains. In this study, from the point of view of grain volume, olivine and augite are considered to be phenocryst, while plagioclase, ilmenite and glass with fine mineral grains are regarded as groundmass. Target bulk density is 3000 kg/m^3, compressive strength is 185 MPa, and tensile strength is 14 MPa, which are considered to be appropriate for mechanical analogs for asteroids (Michikami et al., 2016). The compressional wave velocity is 6.1 km/s, measured using a pulse transition method for a slab sample 1 cm in thickness.

The Sayh al Uhaimir 001 (SaU 001) meteorite (shock stage: S2) from Oman is classified as a L5 chondrite. It is primarily composed of olivine and pyroxene with different grain sizes as crystals in chondrules, recrystallized matrix and mineral fragments (Fig. 1b). The bright grains in Fig. 1b are troilite and Fe–Ni metal. Relatively fine crystals of plagioclase and other minor phases are also present in the recrystallized matrix. Target bulk density is 3400 kg/m^3, the same as Itokawa regolith particles (Tsuchiyama et al., 2011). The compressional wave velocity is 6.6 km/s, measured at Kobe University using a pulse transition method for a cube sample 1 cm in side length. Here, we did not measure the material strength of the L5 chondrite because the total sample volume was small. We can however assume that the material strength is similar to L and LL chondrites (Medvedev et al., 1985) or basalts (e.g., Takagi et al., 1984) because the value of the compressive wave velocity in our sample is similar to those in L and LL chondrites (Yomogida and Matsui, 1983).

2.2. Impact experiments

The impact experiments into two types of target were carried out with a two-stage light-gas gun at the Institute of Space and Astronautical Science, Japan Aerospace Exploration Agency (ISAS, JAXA). A high-speed framing video camera was used to record the impact point of the target surface and the behavior of the ejecta. The frame rate of the camera was set to 4000 frames/s.

For basalt targets, impact experiments have already been carried out by Michikami et al. (2016). A total of 23 impact experiments were carried out by firing a spherical nylon projectile (diameter 7.14 mm, mass 0.217 g and density 1140 kg/m^3) perpendicularly into cubic targets with 5–15 cm side length at velocities of 1.60–7.13 km/s. In all runs, the projectiles hit the center of the targets. More than 12,700 fragments with $b \geq 4$ mm generated in the impact experiments were measured by Michikami et al. (2016). The small fragments with $b < 4$ mm generated in these impact experiments were stored and the small fragments of eight shots were measured in this study. We selected the eight shots from two points of view: (1) The impact velocity was approximately maintained (~5 km/s) while the target size was changed from 5 cm to 15 cm side length (s2129, s2130, s2131 and s2570). (2) The target size was maintained (cubic targets with 7.5 cm side length) while the impact velocity was changed from 1.6 to 7.0 km/s (s2132, s2137, s2128, s2130 and s2126). Target properties and experimental results are summarized in Table 1.

For the L5 chondrite targets, we used a slab (4.0 × 2.3 × 0.67 cm) and cubic (1.0 × 1.0 × 1.0 cm) targets. In shots s3104 and s3105, a spherical alumina projectile (diameter 1.0 mm and mass 0.0036 g) was fired perpendicularly into the targets with impact velocities of 4.90 km/s and 4.97 km/s, respectively. For the slab target (s3104), the impact direction was parallel to the shortest axis of the target, i.e. the projectile was shot into the target surface with the largest area and the projectile hit the upper side 0.7 cm from the center of the target. For the cubic target (s3105), the projectile hit the upper left of the target surface.

Each target was set on a cylindrical stand less than one third of the target size in diameter. The whole system was mounted in a vacuum chamber (almost 1 × 1 × 2 m^3) with acrylic resin windows. The ambient pressure in the chamber was less than 200 Pa. The experiments were carried out with two different experimental setups (for more detail, refer to Michikami et al., 2016). In the first setup (s2126, s2128, s2129, s2130, s2131, s2132 and s2137 in this study), several styrofoam boards 1 cm thick were put on the interior of the chamber to prevent the destruction of fast fragments by secondary collisions on the interior chamber. After the impact, we collected the fine fragments accumulated gently on styrofoam boards and measured the three-dimensional structures of a small number of them by microtomography. We also collected the remaining fine fragments inside the chamber, although their sizes were not measured. In the second setup (s2570, s3104 and s3105 in this study), a cardboard box (59 × 56 × 45 cm^3) was put on the floor of the chamber to prevent the destruction of fast fragments by secondary collisions as well. After the impact, we collected all fragments in the cardboard box and measured the three-dimensional structures of a small amount of the fine fragments by microtomography. A few hundred fragments are enough to investigate their shapes statistically, although numerous fine fragments (often several thousands) per shot were collected in the experiments. Thus, the numbers of fine fragments measured (an arbitrary selection) for individual experiments were from 162 to 352 (Table 1). The size distributions of these fine fragments are shown in Fig. B.1 of Appendix B.

3. Measurement and analysis method for fine fragments

3.1. X-ray microtomography

The fine fragments were imaged at the SPring-8 BL20B2 beamline, Hyogo, Japan, using SR-based X-ray absorption projection tomography (Uesugi et al., 2012). The advantage of X-ray microtomography is that one can obtain three-dimensional sample shapes with μm spatial resolution of samples and their petrographic textures using quantitative absorption contrast (Tsuchiyama et al., 2005). The voxel size of 1.73 μm or 1.74 μm is sufficient for our purposes. In this study, we arbitrarily selected a few hundred fine fragments smaller than 200 μm and measured these, so that they could be compared with Itokawa particles smaller than 120 μm. Therefore, there are only a small number of fragments larger than 200 μm in the tomography measurements, numbers range from a few to approximately fifty on each shot.

A double-sticky carbon tape 0.1–0.2 mm thick and 5.0 × 6.6 mm^2 in size carrying the fragments was attached to an aluminum cylinder 2.1 mm in diameter. The sample was imaged using a monochromatic X-ray beam of 20 or 25 keV. CT images were obtained using 1800 projection images (0.1°/projection). Reconstruction processing made use of a convolution back-projection algorithm (Nakano et al., 2000). Successive CT images of different slices through the particles were then stacked to obtain their 3-D structure.

Minerals in the CT images could be identified because monochromatic X-ray energies were used. Linear attenuation coefficients (LACs) of the relevant standards measured at SPring-8 (Tsuchiyama et al., 2005) were used to obtain the LACs in the CT

Table 1
Sumary of target properties and experimental results. M_t, M_l and Q are initial target mass, largest fragment mass and specific energy, respectively. Fragmentation types are cratering (Type I), transition type (Type II), core type (Type III) and complete destruction (Type IV). The shapes of the fragments with $b \geq 4$ mm (L size), mid-sized fragments 120 μm to 4 mm (M size) and fine fragments less than 120 μm (S size) were obtained from basalt targets by Michikami et al. (2016). The S-sized fragments are divided into three petrographic texture types (Type P, P/G and G). When the p-values of a Kruskal–Wallis test among these of three types (the right column) are less than 0.05, this implies that the differences between these are statistically significant at the 95% confidence level.

	Target			Impact features				Fragments					
Shot number	Material	Dimension (cm)	M_t (g)	Velocity (km/s)	Q (J/kg)	Fragmentation type	M_l/M_t	Size type and petrographic type in S sized fragments	Mean value of b/a	Mean value of c/a	Mean value of c/b	Counted number	p-values of Kruskal–Wallis test among P, P/G and G
s2126	Basalt	7.5 × 7.5 × 7.5	1240.4	6.99	4280	III	0.051	L	0.71	0.41	0.59	1659	
								M	0.73	0.48	0.66	99	b/a: 0.05
								S	0.71	0.50	0.71	241	c/a: 0.01
								P	0.72	0.53	0.75	82	c/b: 0.01
								P/G	0.67	0.48	0.72	51	
								G	0.72	0.49	0.68	108	
s2128	Basalt	7.5 × 7.5 × 7.5	1240.7	3.69	1190	III	0.410	L	0.69	0.39	0.58	338	
								M	0.75	0.50	0.67	34	b/a: 0.28
								S	0.72	0.52	0.72	172	c/a: 0.09
								P	0.73	0.54	0.75	75	c/b: 0.01
								P/G	0.75	0.49	0.66	27	
								G	0.71	0.50	0.71	70	
s2129	Basalt	5 × 5 × 5	360.9	5.32	8540	IV	0.018	L	0.74	0.45	0.62	756	
								M	0.73	0.52	0.72	92	b/a: 0.90
								S	0.72	0.52	0.73	70	c/a: 0.59
								P	0.71	0.53	0.74	27	c/b: 0.60
								P/G	0.73	0.53	0.73	27	
								G	0.72	0.49	0.70	16	
s2130	Basalt	7.5 × 7.5 × 7.5	1227.1	5.27	2470	III	0.088	L	0.71	0.41	0.59	1194	
								M	0.69	0.47	0.69	60	b/a: 0.58
								S	0.73	0.52	0.71	292	c/a: 0.03
								P	0.74	0.55	0.74	88	c/b: 0.06
								P/G	0.74	0.52	0.70	83	
								G	0.73	0.51	0.70	121	
s2131	Basalt	10 × 10 × 10	2948.9	5.32	1050	III	0.211	L	0.71	0.38	0.55	686	
								M	0.73	0.44	0.61	31	b/a: 0.75
								S	0.71	0.51	0.72	275	c/a: 0.02
								P	0.72	0.53	0.74	108	c/b: 0.07
								P/G	0.71	0.50	0.71	53	
								G	0.71	0.49	0.70	114	
s2132	Basalt	7.5 × 7.5 × 7.5	1229.9	1.60	230	I	0.999	L	0.69	0.24	0.38	5	
								M	0.75	0.49	0.67	12	b/a: 0.20
								S	0.72	0.50	0.71	255	c/a: < 0.01
								P	0.72	0.53	0.74	95	c/b: 0.01
								P/G	0.74	0.52	0.71	53	
								G	0.70	0.48	0.68	107	
s2137	Basalt	7.5 × 7.5 × 7.5	1239.7	2.10	390	II	0.961	L	0.68	0.28	0.43	14	
								M	0.67	0.48	0.71	15	b/a: 0.72
								S	0.71	0.49	0.70	215	c/a: 0.17
								P	0.72	0.51	0.71	91	c/b: 0.38
								P/G	0.70	0.47	0.67	44	
								G	0.70	0.49	0.70	80	
s2570	Basalt	15 × 15 × 15	10,031.0	5.01	270	II	0.944	L	0.71	0.26	0.38	118	
								M	0.71	0.44	0.62	32	b/a: 0.44
								S	0.72	0.50	0.71	238	c/a: 0.07
								P	0.73	0.52	0.73	88	c/b: 0.25
								P/G	0.70	0.48	0.70	56	
								G	0.72	0.49	0.69	94	
s3104	L5 chondrite	4.0 × 2.3 × 0.67 *slab	21.7	4.90	1930		0.124	M	0.71	0.45	0.64	93	
								S	0.72	0.52	0.72	113	
s3105	L5 chondrite	1.0 × 1.0 × 1.0	3.4	4.97	13,540		0.051	M	0.71	0.45	0.64	39	
								S	0.71	0.52	0.74	292	

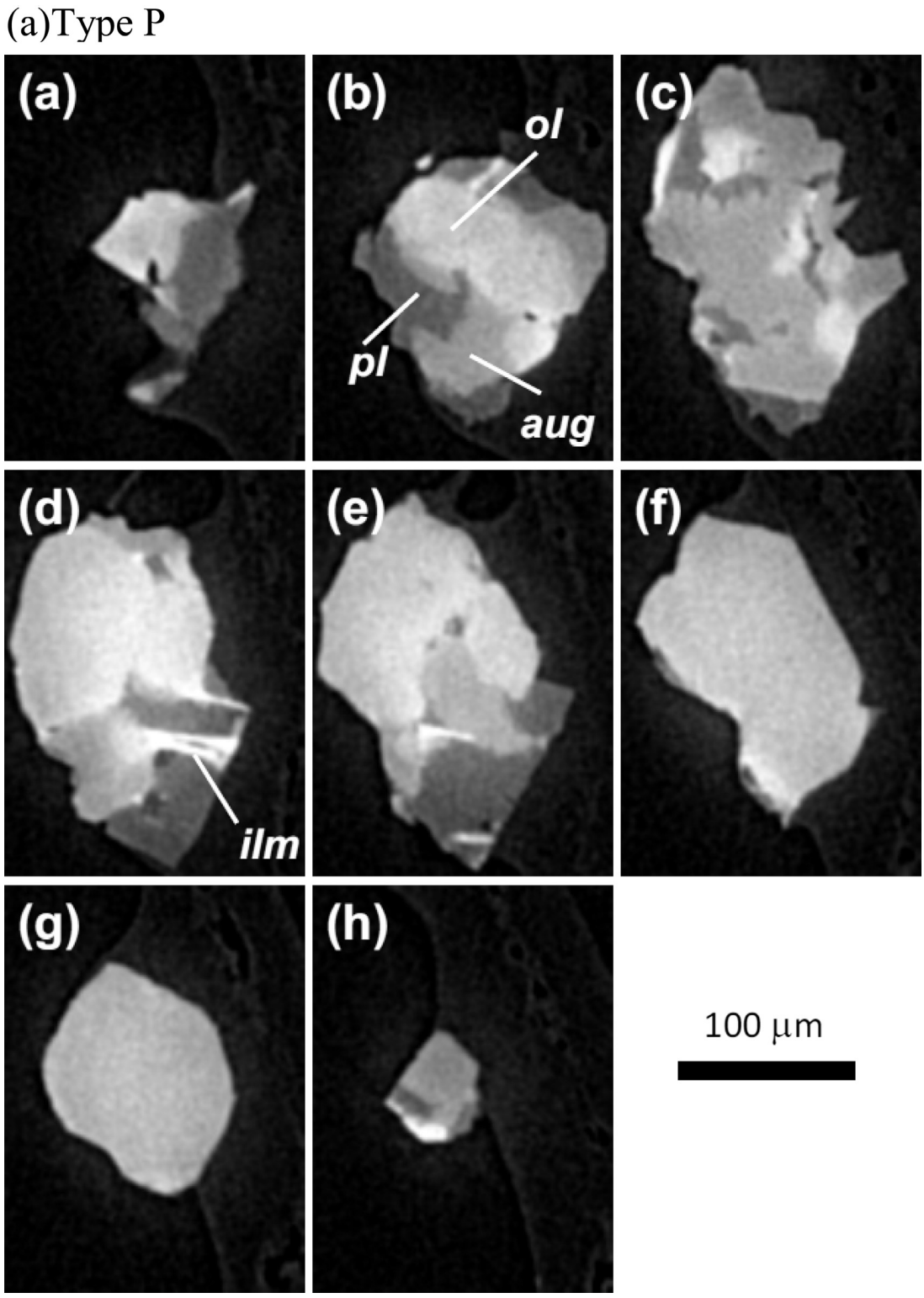

Fig. 2. Sequence of slice images of 3D CT image stacks in every 34 μm for typical fine basalt fragments obtained by microtomography. (a–h) Type P, phenocryst-rich fragment. (i–q) Type P/G, intermediate fragment. (r–z) Type G, groundmass-rich fragment. Mineral abbreviations are the same as in Fig. 1.

images, which helped to derive mineralogical identifications such as olivine, pyroxene, and plagioclase.

3.2. Image analysis

The "Slice" software package (Nakano et al., 2006) was used for 3-D CT image analysis. The relevant method was described in previous studies (Tsuchiyama et al., 2011, 2014). A solid object was extracted three-dimensionally by binarization of the CT images as individual particles. The binarization thresholds were determined by eye based on the CT images of each data set. This value is close to the half of the LAC value that corresponds to the sample peak in the LASC histogram. Relative values of the three-axial length and

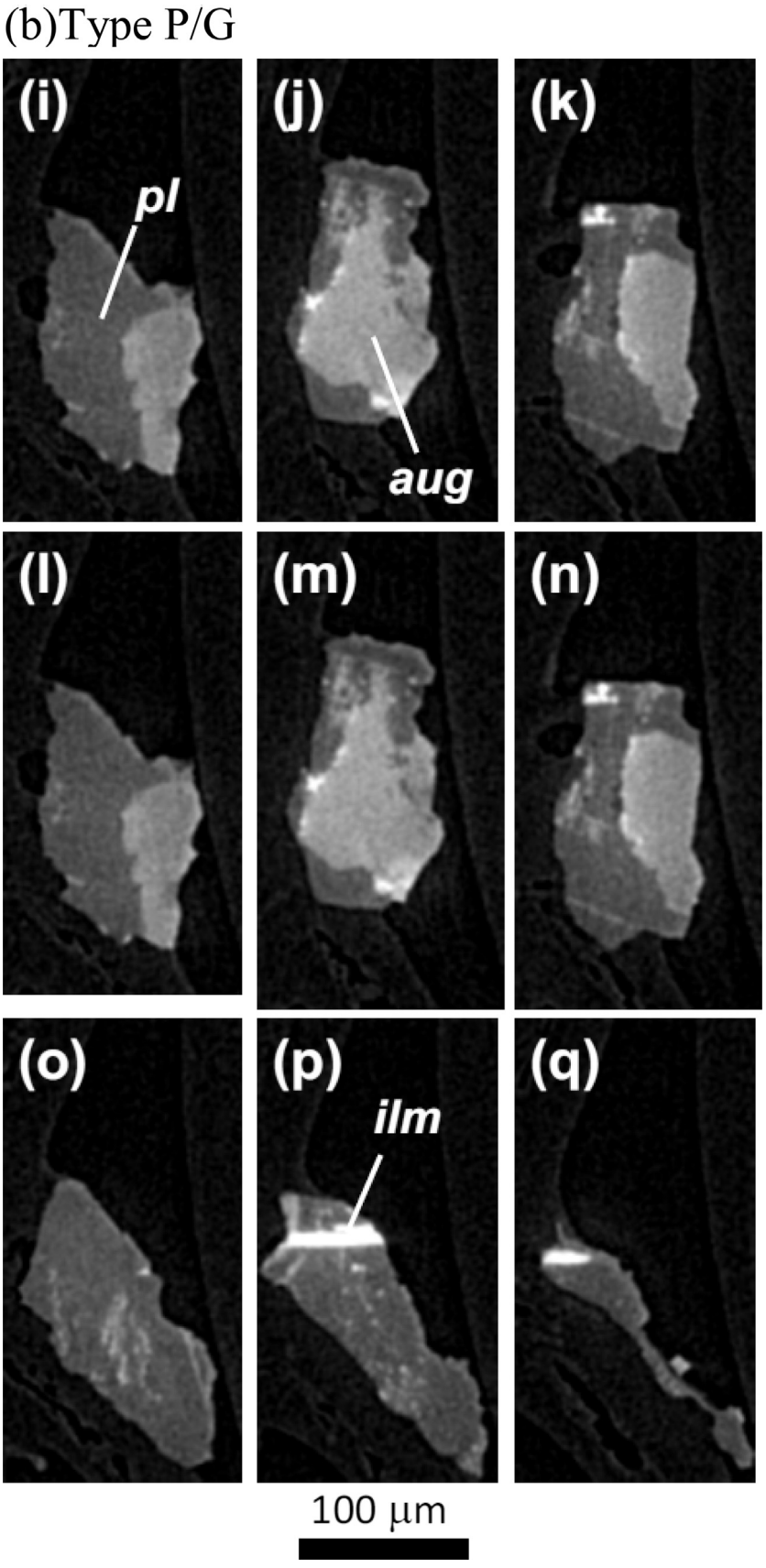

Fig. 2. Continued

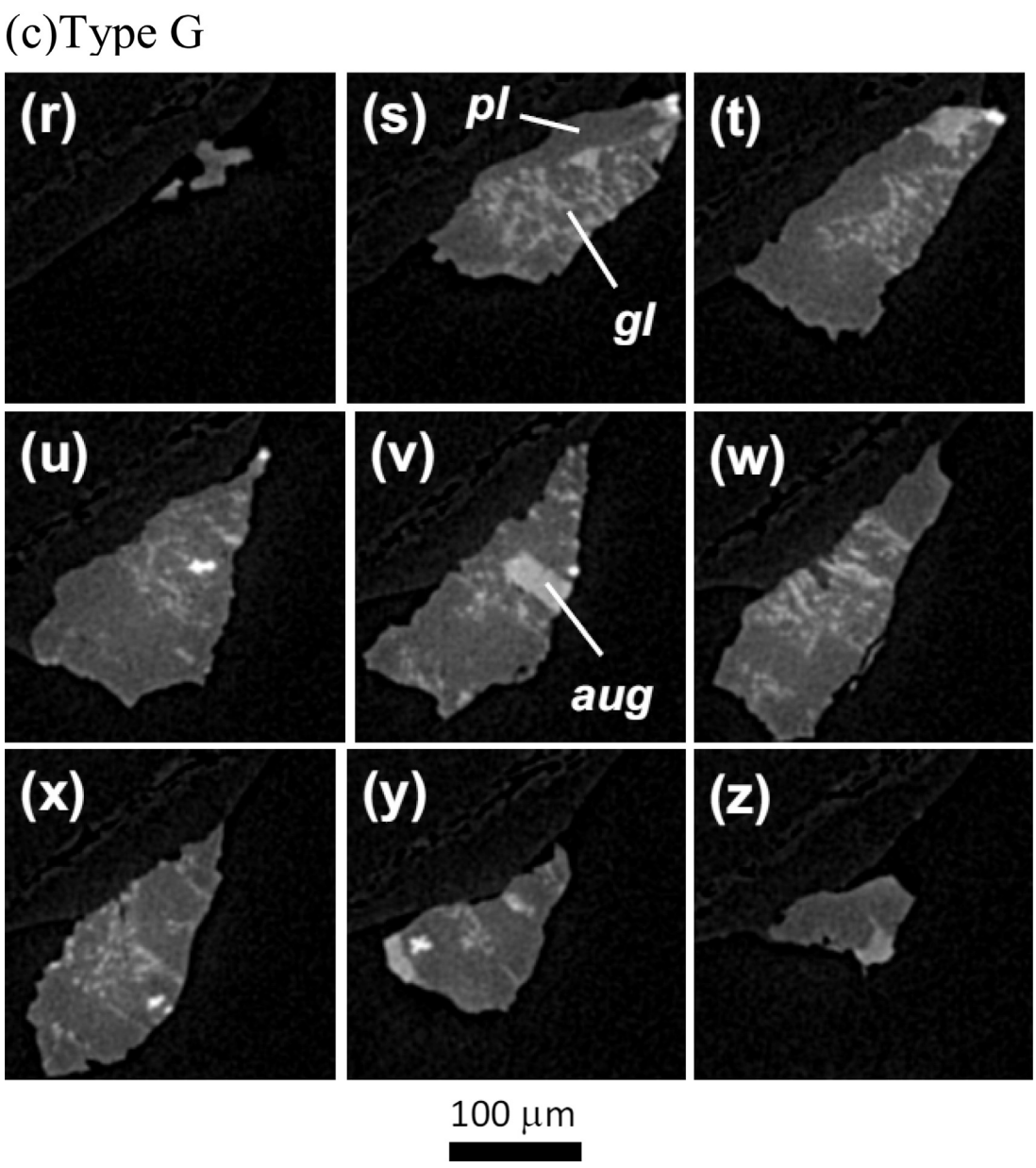

Fig. 2. Continued

thus the three-axial ratio were not largely changed by the threshold value.

The CT images were processed to yield a solid object in three dimensions. We checked whether or not the grains are in contact with each other for all the fragments in the CT images. Grains in contact were eliminated from further analysis and only separated grains were analyzed. Then their volumes were calculated from voxel size and number on the solid object. We used the sphere-equivalent diameter, calculated from the particle volume, to define the size of these small fragments. Fine fragments smaller than 10,000 voxels were omitted because their axial ratios can be difficult to determine accurately. The smallest fine fragments were approx. 46 μm.

The three axial dimensions, *a, b*, and *c* ($a \geq b \geq c$) of the fine fragments were measured using software developed in this study employing the method of rotating calipers through the extraction of a convex hull of particles. In this study, *a, b*, and *c* are defined as the dimensions of a fragment in three mutually orthogonal planes. The algorithm started by measuring the shortest dimension of the fragment, and then the shortest dimension perpendicular to this and, finally, the dimension perpendicular to both (*BU* method, see Appendix A). The fragment measurement method corresponds to that manually applied by Fujiwara et al. (1978) and Michikami et al. (2016) for fragments larger than $b \geq 4$ mm in previous studies. It is noted that, because the definitions of the fragment shapes are not unique in previous studies, we discuss the resulting differences in the measurement methods in Appendix A.

As mentioned above, because the relation between the petrographic textures and the shapes of fine fragments is the subject of this study, we classified the fine basalt fragments into three types by eye, based on their CT images (Fig. 2):

Type P, phenocryst-rich, more than ~¾ by volume consists of phenocryst composed of olivine and augite;
Type P/G, intermediate, with approximately equal volume fractions of phenocryst and groundmass;
Type G, groundmass-rich, where only ~¼ by volume consists of phenocryst and more than ~¾ by volume is made up

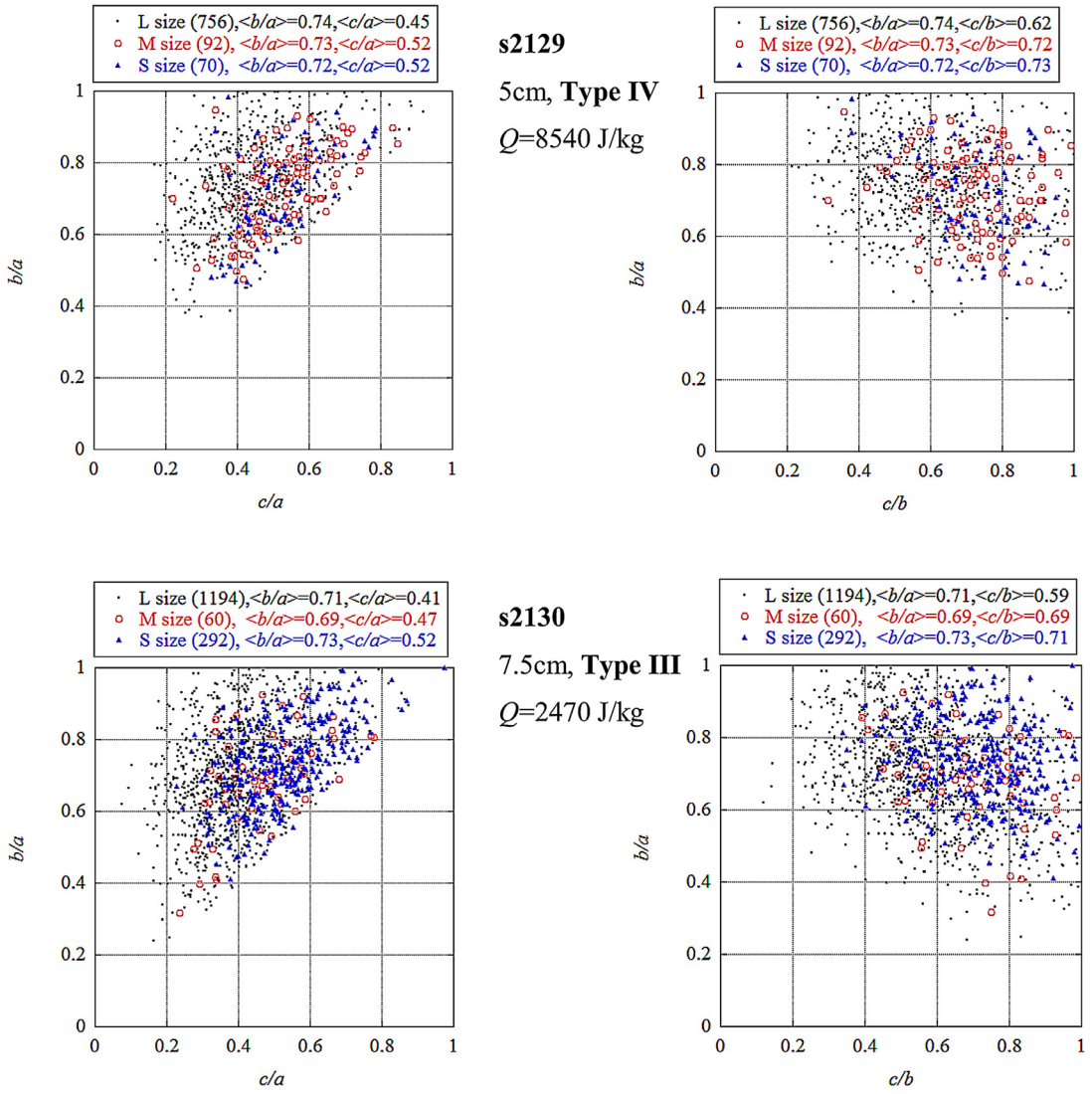

Fig. 3. Diagrams (s2129, s2130, s2131, s2132 and s2570) for the shape distributions of relatively large fragments with $b \geq 4$ mm (L size), mid-sized fragments with 120 μm–4 mm (M size) and fine fragments smaller than 120 μm (S size) obtained from the basalt targets by Michikami et al. (2016). In the data for M and S sizes, we used the sphere-equivalent diameter to define fragment size. The axial ratio *b/a* vs *c/a* is shown on the left and *b/a* vs *c/b* is shown on the right. These data were obtained by keeping approximately same impact velocity (~5 km/s) with target size varying between 5 cm and 15 cm side length (s2129, s2130, s2131 and s2570), except for shot s2132, where impact velocity was 1.60 km/s and the target size was 7.5 cm side length. Target size, fragmentation types and *Q* value are shown between columns. The number of fragments in each size group is given in parentheses and mean *b/a*, *c/a* and *c/b* are indicated in square brackets.

of groundmass composed of plagioclase, ilmenite, glass and fine mineral grains.

4. Results

4.1. Basalt

4.1.1. Degree of fragmentation and fragment shapes

In the adopted experimental data of the fragments (Michikami et al., 2016), the degrees of fragmentation of the target are observed in a wide range from cratering to catastrophic disruption. A specific energy, *Q*, defined as the kinetic energy of the projectile per unit target mass, is a widely-used measure that indicates target fragmentation in laboratory studies and numerical simulations (e.g., Holsapple et al., 2002). In line with Michikami et al. (2016), we grouped the degrees of fragmentation of the target into four types in the order of decreasing *Q*:

Type I, cratering with no catastrophic disruption [$Q < 250$ J/kg] (shot, s2132);

Type II, a transition type where parts of the side surfaces are chipped off [$250 \leq Q < 1050$ J/kg] (shots, s2137 and s2570);

Type III, the so-called core type, signified by whole surfaces of the target being spalled off with only the core in the central part of the target remaining [$1050 \leq Q < 8000$ J/kg] (shots, s2126, s2128, s2130 and s2131); and

Type IV, complete destruction, in which the targets are completely destroyed into fine fragments and no core is left [8000 J/kg $\leq Q$] (shot, s2129).

Fig. 3 shows the diagrams (s2129, s2130, s2131, s2132 and s2570) for the shape distribution of relatively large fragments with $b \geq 4$ mm (L size), mid-sized fragments 120 μm to 4 mm (M size) and fine fragments less than 120 μm (S size) obtained from basalt targets by Michikami et al. (2016). The impact velocity was approximately maintained (~5 km/s) while the target size was changed from 5 cm to 15 cm side length (s2129, s2130, s2131 and s2570), with the exception of shot s2132, where the impact velocity was 1.60 km/s and target side length was 7.5 cm. Impact velocities of ~5 km/s correspond to the mean collisional velocity among the

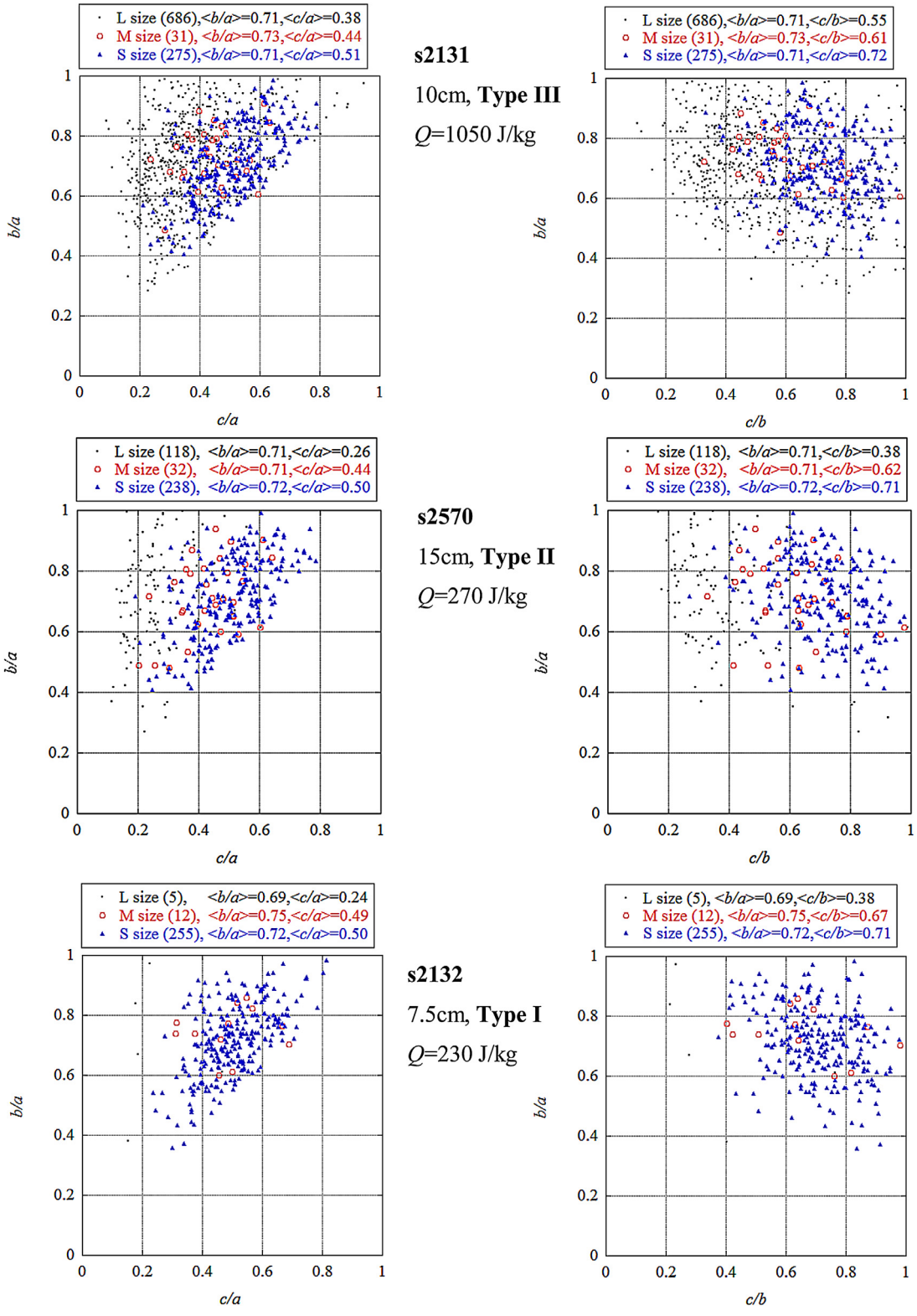

Fig. 3. Continued

main belt asteroids. Shot s2129 is of Type IV (complete destruction), s2130 and s2131 are Type III (core type), and s2570 is Type II (transition type). As target size did not exceed 15 cm, fragmentation of Type I (impact cratering) was not observed in the experiments with an impact velocity of ~5 km/s. To illustrate impact experiments of Type I, we added the data of s2132 with an impact velocity of 1.60 km/s to the experimental data.

We have chosen two different graphical representations of the fragment shape data in terms of the three axial ratios: *b/a* vs *c/a* and *b/a* vs *c/b*. The former type of plot was used by Fujiwara et al. (1978), Capaccioni et al. (1984, 1986) and Michikami et al. (2016) in their studies of laboratory impact experiments. Plots of the latter type were used in the analysis of Itokawa regolith and LL chondrite particles by, e.g., Tsuchiyama et al. (2011, 2014), and of Lunar

regolith particles by Katagiri et al. (2014). In the present study, we adopted both types of plot in order to compare both fine and relatively large laboratory fragments and also Itokawa regolith particles.

As shown in Fig. 3, the distributions of shapes of M- and S-sized fragments seem to be similar both in terms of the spread and mean axial ratios despite the difference in their size distributions (Appendix B; Fig. B.1). That is, most fragments with M and S sizes lie in the region of the diagram defined by $0.9 > b/a > 0.5$ and $c/a > 0.25$ (or $c/b > 0.5$), and the mean b/a, c/a and c/b ratios in these experiments are similar, approximately 0.7, 0.5 and 0.7, respectively (although the mean c/a and c/b ratios of M-sized fragments are slightly smaller than those of S-sized fragments). In a Kruskal–Wallis test, a suitable test for confirming the difference between more than three statistical populations with non-normal distributions, the p-values among these mean axial ratios in S-sized fragments are 0.28 for b/a, 0.53 for c/a and 0.60 for c/b. Because these p-values in the Kruskal–Wallis test are greater than 0.05, the differences among these mean axial ratios in S-sized fragments are not statistically significant at the 95% confidence level. Therefore, we conclude from our experiments that the degree of fragmentation does not affect the shapes of fine fragments smaller than 120 μm.

On the other hand, the shapes of L-sized fragments are influenced by the degree of fragmentation as already pointed by Michikami et al. (2016), i.e. the mean c/a and c/b ratios decrease with decreasing the specific energy, Q. Besides, the spread of these shape distributions is large compared with the distributions of M- and S-sized fragments. In Type IV impacts, almost all the fragments lie in the region of the diagram (histogram) defined by $b/a > 0.4$ and $c/a > 0.2$. In Type III, II and I impacts, the number of fragments in the region of the diagram defined by $c/a \leq 0.2$ slightly increases, decreasing with the degree of fragmentation (i.e. decreasing with the specific energy, Q). Therefore, the shapes of L-sized fragments differ from M- and S-sized fragments. This applies even when the shapes of the fragments of catastrophic disruptions are compared. For example, a Kruskal–Wallis test of shot s2129 shows that the differences among the mean axial c/a and c/b ratios in L-, M- and S-sized fragments are statistically significant at the 95% confidence level (Both p-values are less than 1×10^{-4}).

In M- and S-sized fragments, the tendency for the mean c/a ratios to remain constant independent of the degree of fragmentation was also found from our other experiments with impact velocities of 2.10–6.99 km/s and targets with identical 7.5 cm side length (s2137, s2128 and s2126) (Table 1).

In order to investigate the relationship between the fragment shape and the degree of the fragmentation, the mean axial ratios are plotted against Q (Fig. 4). Fig. 4 indicates that the mean b/a ratios of fragments of all sizes seem to be approximately constant regardless of Q, or seem to slightly decrease with decreasing Q. On the other hand, for L-sized fragments, the mean c/a ratios decrease gradually with decreasing Q when $Q < 1000$ J/kg. However, for M- and S-sized fragments, the mean c/a ratios are constant, as mentioned before. The mean c/a ratio of M- and S-sized fragments is greater than the corresponding ratio of L-sized fragments, and the mean c/a ratio of M-sized fragments seems to lie between L- and S-sized fragments. This difference will be discussed in Section 5.

4.1.2. Petrographic textures and fine fragment shapes

As mentioned before, it is possible that the petrographic textures and the crystal grain boundaries affect the shapes of S-sized fragments because their sizes are comparable to or greater than the sizes of fragments. In order to investigate the relation between the petrographic textures and the shapes of S-sized fragments, the shape distributions of the three aforementioned petrographic types (P, P/G and G) are shown in Fig. 5. Overall, the distributions seem to be similar both in terms of the spread and mean axial ratios; the axial ratios of fragments for each type are distributed around mean values of the axial ratios $b/a \sim 0.7$ and $c/a \sim 0.5$. In each shot, the values of a Kruskal–Wallis test among three mean axial ratios are indicated in Table 1. All shots in terms of b/a show that the differences are not statistically significant at the 95% confidence level. On the other hand, their half numbers of shots in terms of c/a show that the differences are statistically significant at the 95% confidence level. However, at the 99% confidence level, almost all shots (except for shot s2132) in terms of c/a indicate that the differences are not statistically significant. In addition, all shots in terms of c/b show that the differences are not statistically significant at the 99% confidence level. Therefore, a Kruskal–Wallis test shows that the petrographic textures and the crystal grain boundaries do largely not affect the shapes of S-sized fragments.

To be more precise, although the values of the mean c/a ratios are almost 0.5, their values slightly decrease in the order of P, P/G and G types, as the ratio of groundmass increases (except for shot s2570). In the basalt targets, the groundmass is mostly composed of plagioclase and some ilmenite. As plagioclase before impact originally is lath or slab-shaped, the original plagioclase would have extreme values in terms of b/a and c/a (e.g., $b/a \sim 0.1$ for lath and $c/a \sim 0.1$ for thin slab). The original shape of ilmenite is more elongated than plagioclase. Nevertheless, the mean b/a and c/a ratios in the fragments after impact are constant, 0.7 and 0.5, respectively. Therefore, from this fact and the results of a Kruskal–Wallis test, we conclude that the shapes of S-sized frag-

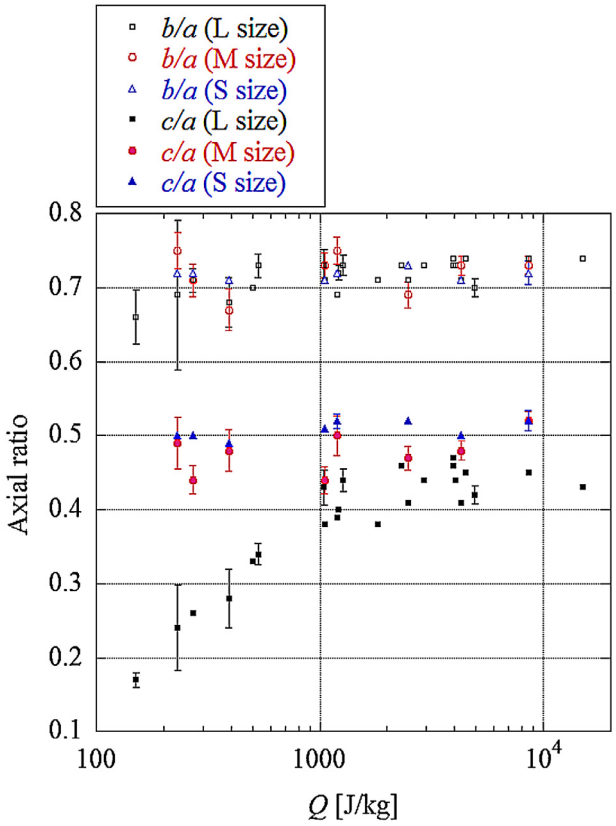

Fig. 4. Mean b/a and c/a ratios vs Q. The data of relatively large fragments with $b \geq 4$ mm (L size) are obtained from the 23 impact experiments on cubic targets, and cover a wide range of Q (150–15,000 J/kg) in Michikami et al. (2016). The data of the mid-sized fragments with 120 μm–4 mm (M size) and the fine fragments smaller than 120 μm (S size) are obtained from 8 of these impact experiments on cubic targets. The standard error bar of each shot is given. In the case of small (i.e. <0.01) standard errors, the error bar is smaller than the symbol size.

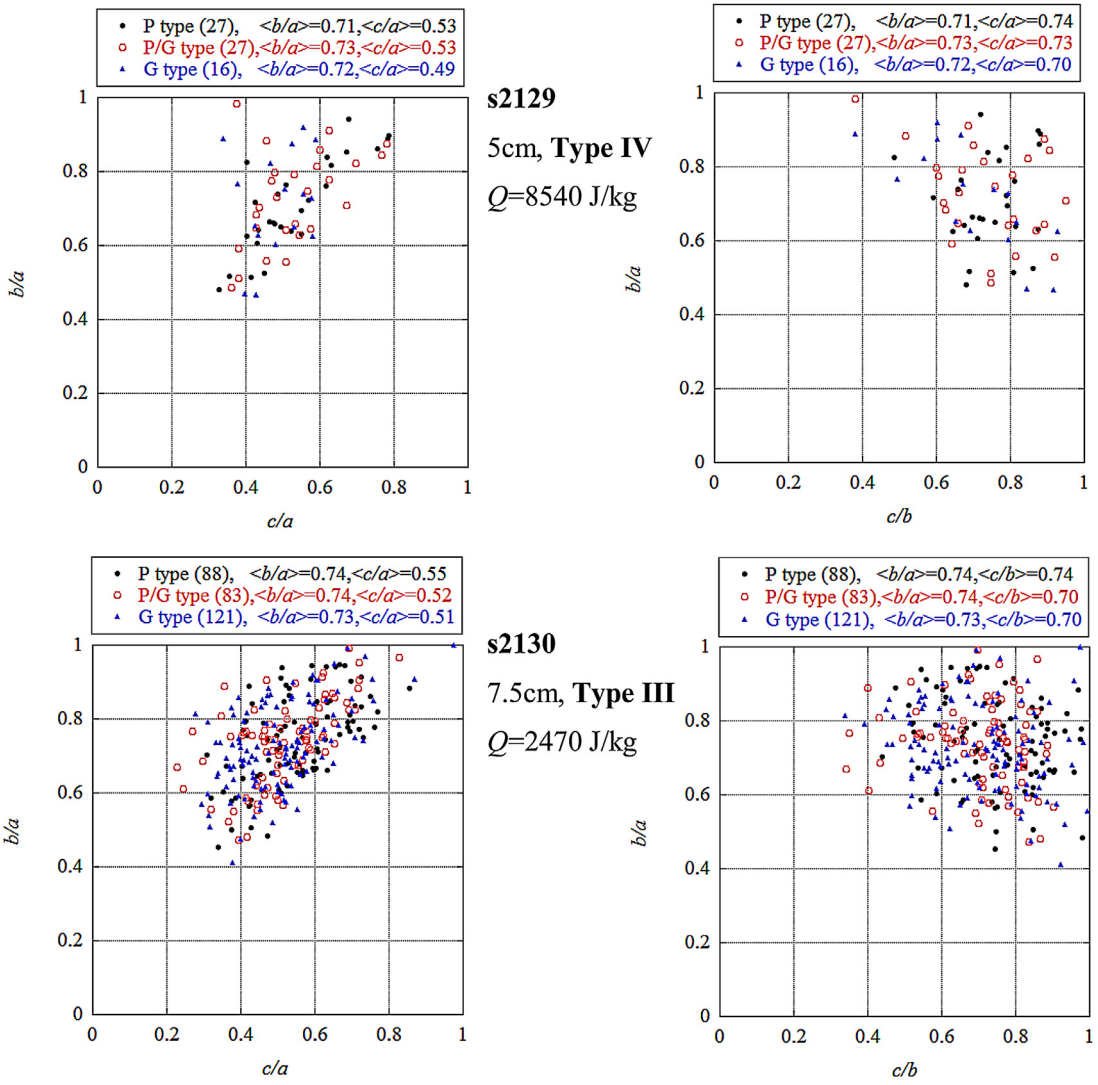

Fig. 5. Diagrams (s2129, s2130, s2131, s2132 and s2570) for three types (P, P/G and G types) of petrographic textures in the shape distributions of fine fragments smaller than 120 μm (S size) obtained from the basalt targets investigated by Michikami et al. (2016). The axial ratio *b/a* vs *c/a* is shown on the left and *b/a* vs *c/b* is shown on the right. The diagrams represent the S-sized fragments data shown in Fig. 3 divided into three types. Target size, fragmentation type and *Q* value are shown between the columns. The number of the fragments in each size group is given in parentheses and mean *b/a, c/a* and *c/b* are indicated in square brackets.

ments are generally not affected by petrographic textures or crystal grain boundaries.

4.2. L5 chondrite

The shape distributions of L5 chondrite as better analogues for the Itokawa regolith particle are indicated in Fig. 6. In Fig. 6, the ratio of the mass of the largest fragment to the initial target mass (M_l/M_t) is given together with the respective shot number as an indicator of target fragmentation instead of a specific energy *Q*. This is because the projectiles in these shots did not hit the center of the target surface and thus a specific energy *Q* would not be a suitable indicator of target fragmentation. (In the shots into basalt targets, all projectiles hit the center of the target surface.) The values of M_l/M_t in shot s3104 (L5 chondrite, slab) and s3105 (L5 chondrite, cube) are 0.12 and 0.05, respectively. In the case of the basalt targets investigated by Michikami et al. (2016), M_l/M_t values of 0.12 and 0.05 correspond to target fragmentations with $Q \sim 2000$ J/kg and $Q \sim 4000$ J/kg or larger, respectively.

The shape distributions of L5 chondrite impact fragments and the basalt target fragments seem to be similar, both in terms of the spread and mean axial ratios: most fragments lie in the region of the diagram defined by $0.9 > b/a > 0.4$ and $c/a > 0.2$ (or $c/b > 0.4$), and the mean *b/a, c/a* and *c/b* ratios in these experiments are similar, approximately 0.7, 0.5 and 0.7, respectively (although M-sized fragments have slightly lower mean *c/a* and *c/b* ratios than S-sized fragments). In a Kruskal–Wallis test, the *p*-values among these mean axial ratios in S-sized fragments (s2129, s2130, s2131, s2132, s2570, s3104 and s3105) are 0.45 for *b/a*, 0.43 for *c/a* and 0.13 for *c/b*. The result indicates that the differences among these mean axial ratios in S-sized fragments are not statistically significant at the 95% confidence level. Hence, just like basalt targets, L5 chondrites (SaU 001) do not show any effect of the degree of fragmentation on the shapes of S-sized fragments.

5. Discussion

5.1. Comparison with previous experiments

In our experiments (Fig. 4), the shapes of S-sized fragments smaller than 120 μm are distributed around mean values of the ax-

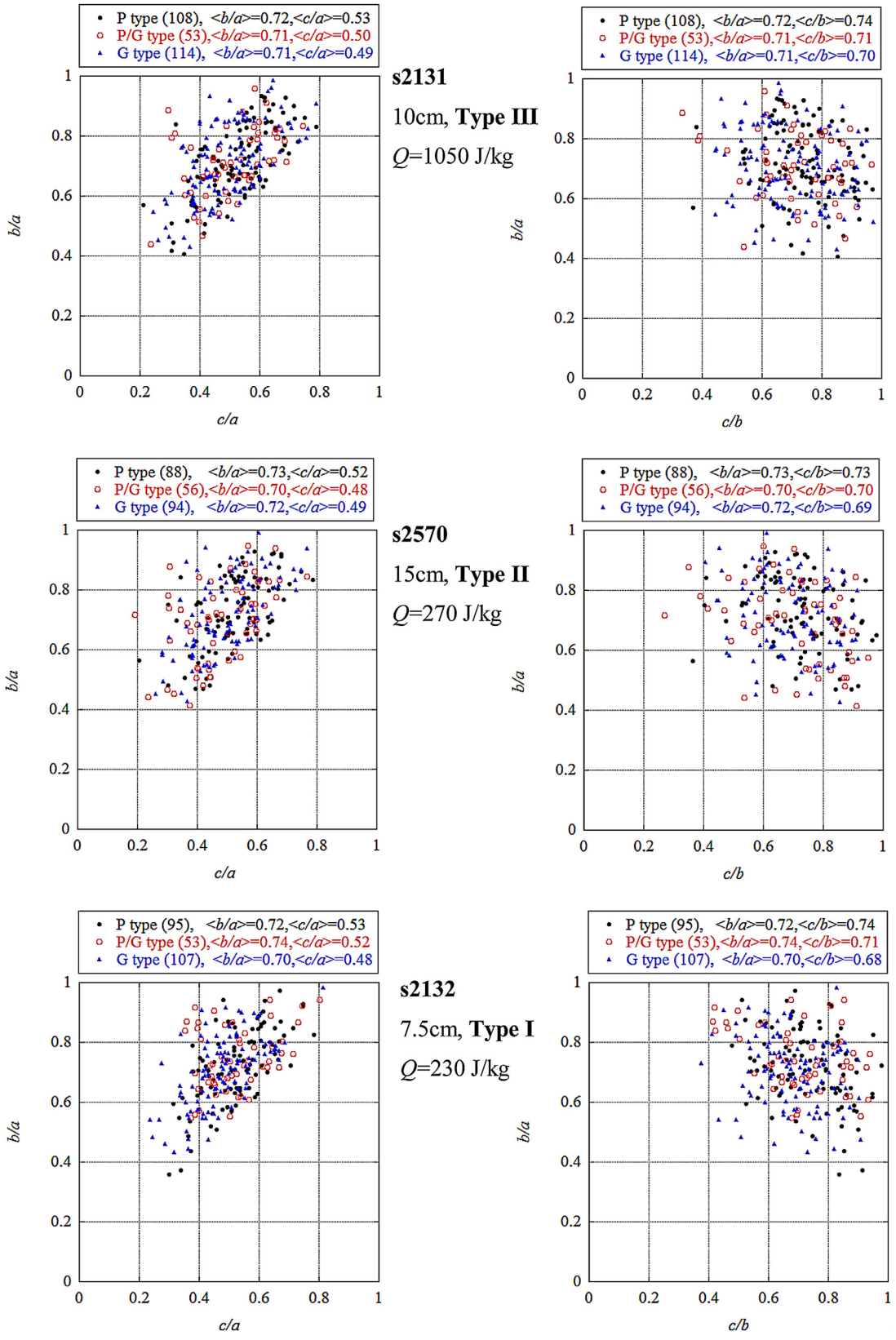

Fig. 5. Continued

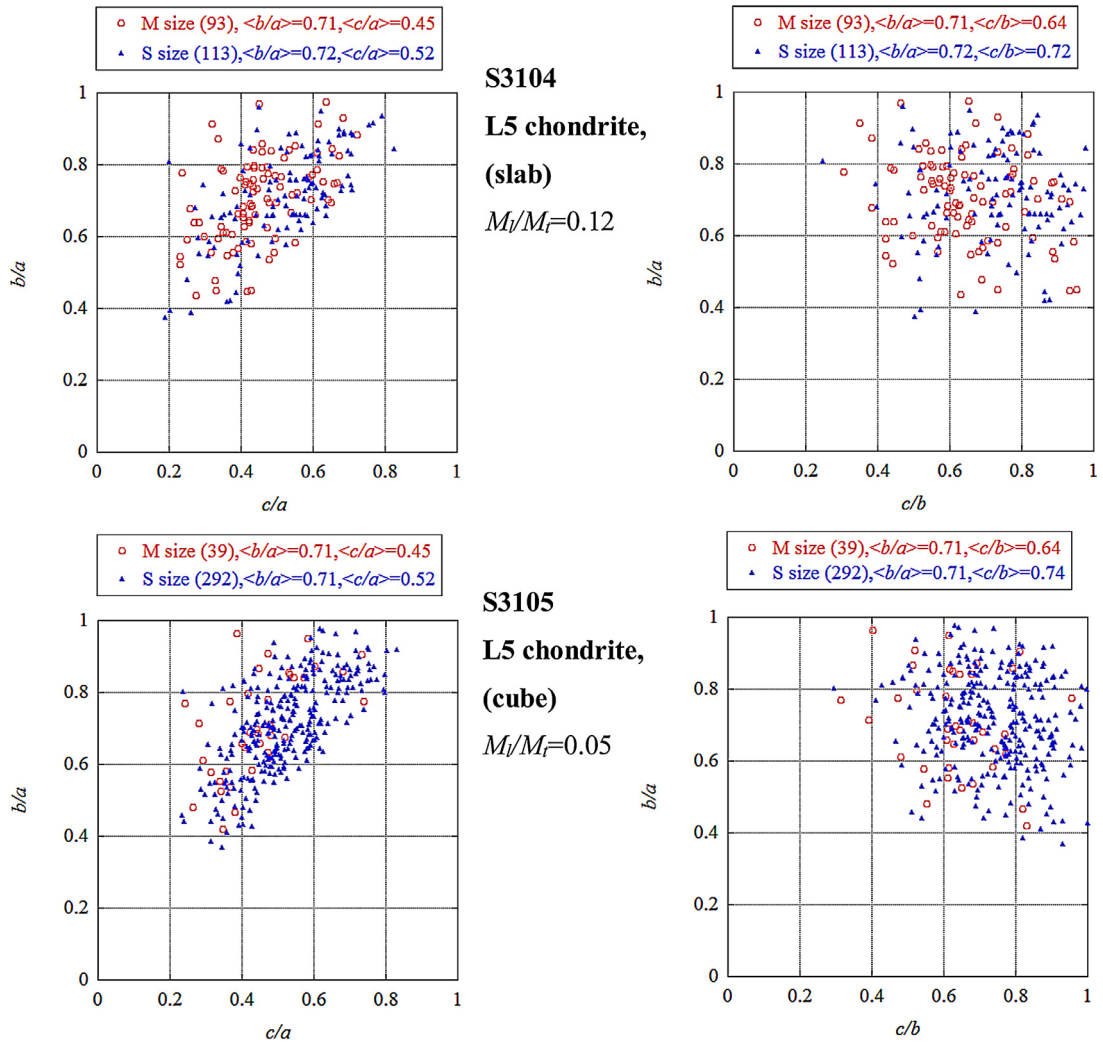

Fig. 6. Diagrams for the shape distributions of M- and S-sized fragments obtained from L5 chondrites. The mass ratio of the mass of the largest fragments to the initial target mass (M_l/M_t) are given beween the columns. The number of the fragments in each size group is given in parentheses and, the mean *b/a*, *c/a* and *c/b* are indicated in square brackets.

ial ratios $b/a \sim 0.7$ and $c/a \sim 0.5$, i.e. corresponding to *a:b:c* in the simple proportion $2:\sqrt{2}:1$, regardless of the specific energy, *Q*. On the other hand, the shapes of L-sized fragments larger than 4 mm examined by Michikami et al. (2016) are dependent on *Q*, and are largely different from those of S-sized fragments; in the case of high *Q*, the mean *b/a* and *c/a* ratios are approximately 0.7 and 0.5, respectively: in the case of low *Q*, the mean *c/a* ratio is small while the mean *b/a* ratio remains approximately 0.7. For instance, in the case of an impact cratering event (low *Q*), the mean *c/a* ratio is nearly 0.2.

In most studies investigating fragment shape to date, the impact experiments were carried out under the condition of high specific energy, *Q* (Fujiwara et al., 1978; Matsui et al., 1982, 1984; Bianchi et al., 1984; Capaccioni et al., 1984, 1986; Durda et al., 2015). The corresponding fragments are larger than several mm and their shapes, in terms of the three axial ratios (i.e. $a:b:c = 2:\sqrt{2}:1$), are similar. As one exception, Capaccioni et al. (1986) have investigated the fragment shapes of smaller fragments, namely down to sizes of the order of 0.1 mm, and the mean axial ratios were the same.

Why do the mean *b/a* and *c/a* ratios of S-sized fragments remain constant regardless of *Q*? We think that the difference in fragment size compared with previous experiments is significant. In previous experiments, unfortunately, there is little evidence for a correlation between size and shape of the fragments. Previous studies even suggested that fragment shapes do not depend on fragment size (e.g., Capaccioni et al., 1986; Michikami et al., 2016). However, the data of previous experiments cover only one or two orders of magnitude in terms of size and the shapes of impact fragments with ~100 μm or less were not measured. For instance, Capaccioni et al. (1986) have collected a sample of 131 fragments in the size range 0.1–1 mm and have imaged them by electron microscope, however, there are only few fragments as small as 0.1 mm. Also, Michikami et al. (2016) did not rule out that fragment size influences fragment shape because of the small size range of fragments investigated. The experimental data used in this study (including the data of Michikami et al. (2016)) cover almost four orders of magnitude in terms of size and we measured the shapes of fragments down 40 μm in size.

One possible explanation for the mean *b/a* and *c/a* ratios of S-sized fragments remaining constant regardless of *Q* that we cannot definitely rule out is secondary fragmentation, namely that fragments break again when they hit the interior surface of the chamber. If most fine fragments were affected by secondary fragmentation, this would take place preferentially along the longest axes. This would increase the mean values of measured ratios (e.g.,

La Spina and Paolicchi, 1996), i.e. the mean *b/a* and *c/a* ratios close to 0.7 and 0.5, respectively, even when the shapes of fragments just before secondary fragmentation are flatter. However, in our experiments, we used a relatively large chamber and Styrofoam boards or a cardboard box, which should effectively prevent destruction by secondary collisions of fragments. Some images of the high-speed camera show that L-sized fragments originating from the targets were not broken when they hit the Styrofoam boards or cardboard box. Although the images of the high-speed camera do not allow us to investigate whether or not secondary fragmentation occurs in S-sized fragment, we believe that S-sized fragments, at least those collected, did not experience secondary fragmentation. This is because only S-sized fragments accumulated gently on Styrofoam boards or the cardboard box were collected in this study.

For a plausible explanation, multiple rarefaction waves in the target are likely to occur when S-sized fragments are formed, thereby determining their shapes. This is because, as mentioned before, fragments are generally produced during the development of the rarefaction wave, in particular fine fragments would be the products of a more complicated destruction as a result of multiple rarefaction waves in the targets (e.g., Fujiwara, 1980; Kadono and Arakawa, 2002). Most large fragments on the other hand might be produced as a result of single or double rarefaction waves in the targets and would be influenced by *Q* and target shape. For instance, during impact cratering (low *Q*), a compressive elastic pulse generally expands radially into the target, and this pulse reflects at the free surface of the target as a rarefaction pulse. Relatively large fragments such as spalled ones ejected from the surface due to single rarefaction wave become fatter. On the other hand, fine fragments might have experienced multiple rarefaction waves even when *Q* is small. The impact experiments for thin glass plates by Kadono and Arakawa (2002) showed that cracks coalesce with each other and become net-like at small scales. Consequently, the formation behavior of fine fragments becomes fractal and the size distribution of fine fragments indicates power-law form (e.g., Meakin, 1984; Kadono and Arakawa, 2002; Aström, 2006). When *Q* is large, multiple rarefaction waves and crossing of pulses with sufficient intensity give a more complicated destruction (Fujiwara, 1980) and as a result the mean *b/a* and *c/a* of L-sized fragments become 0.7 and 0.5, respectively. Therefore, the fragment shape is considered to be strongly influenced by the pattern of the rarefaction wave in the target during impact. The S-sized fragments with a regular shape regardless of *Q* would be produced by multiple rarefaction waves in the target.

5.2. Comparison with Itokawa regolith particles and implications

In Fig. 7, the shape distributions resulting from basalt and L5 chondrite impacts are compared with that of 41 Itokawa regolith particles of Tsuchiyama et al. (2014). Note that, out of the 48 Itokawa regolith particles Tsuchiyama et al. (2014) investigated we excluded 7 particles confirmed to be pieces of original particles fragmented during curation, as indicated by a branch number (an additional 1–2 digits) in their sample ID (e.g., RA-QD02-0062-01; see Table 1 in Tsuchiyama et al., 2014). Moreover, the shape of these Itokawa particles was newly determined using the *BU* method instead of the *EA* method (see Appendix A) for comparison with the results of the present experiments. In the data of basalt targets in Fig. 7, we used data of the shots with minimum and maximum *Q* (230 J/kg in s2132 and 8540 J/kg in s2129).

The shape distributions in Fig. 7 seem to be similar both in terms of spread and mean axial ratios although the mean *b/a* ratio of Itokawa particles is slightly larger and the mean *c/a* and *c/b* ratios of Itokawa particles are slightly smaller when compared basalt and L5 chondrite fragments. In a Kruskal–Wallis test, the *p*-values are 0.67 for *b/a*, 0.37 for *c/a* and 0.15 for *c/b* for these data. This means that the differences among these mean axial ratios are not statistically significant at the 95% confidence level. Therefore, we conclude that the shape distribution of the Itokawa particles is similar to those of the laboratory experimental fragments obtained from basalt and L5 chondrites.

The finding that the shape distributions of the Itokawa particles and the laboratory impact fragments smaller than 120 μm are similar is a clue for the formation of Itokawa particles. Tsuchiyama et al. (2011) suggested that the Itokawa particles are impact fragments on the asteroid surface, based on the shape distribution. Also, the investigation of sub-micro craters on the surface of Itokawa particles indicates that these craters are considered to be secondary ejecta craters that resulted from fragments impacting on the Itokawa regolith (Matsumoto et al., 2016; Harries et al., 2016). Thus, previous studies suggest that the Itokawa particles are impact fragments on the asteroid surface or were at least strongly influenced by impact phenomena.

As mentioned above in our experiments, neither petrographic textures nor crystal grain boundaries significantly affect the shapes of S-sized impact fragments. In basalts, the phenocrysts do not significantly affect fragment shapes (even for M-sized fragments). On the other hand, in L5 chondrites, it is possible that the chondrules affect the shapes of M-sized or larger fragments because these sizes are comparable. For instance, in the case of the size distribution, hypervelocity impact experiments on ordinary chondrites by Flynn and Durda (2004) showed a bend in the mass frequency distribution of the fragments at approximately the mass of the chondrules, suggesting that the presence of chondrules altered the distribution. However, in our experiments, the shapes of M- and S-sized fragments in basalts are similar, and the shapes of M- and S-sized fragments in L5 chondrites are not very different. Therefore, we think that the shapes of neither M- nor S-sized impact fragments in basalts and L5 chondrites are significantly affected by petrographic textures or crystal grain boundaries. In the future, a more quantitative investigation of the influence of chondrules on the shape of larger than mm-sized particles would be needed.

The Itokawa particles smaller than 120 μm, which would be produced by impacts, are also considered not to be influenced by the petrographic textures and the crystal grain boundaries because their shape distributions of polymineralic and monomineralic particles are similar (Tsuchiyama et al., 2011, 2014). On the other hand, in thermal fatigue caused by the day-night temperature cycles on an asteroid surface, amplification of stress occurs at surface-parallel boundaries between adjacent mineral grains as a result of the difference in thermoelastic behavior between adjacent grains (Molaro et al., 2015). Therefore, the petrographic textures and the crystal grain boundaries would affect the shapes of the fragments produced by such a thermal fatigue. If the Itokawa regolith particles were produced by thermal fatigue, their shape distribution would be influenced by their petrographic textures and crystal grains, and their shapes would be different from laboratory impact fragments in our experiments. However, since the shapes of the Itokawa particles are similar shapes to the laboratory impact fine fragments, we concluded that the Itokawa particles are not produced by thermal fatigue and are therefore impact fragments on the asteroid surface. Note that this conclusion has not been found in previous studies (e.g., Tsuchiyama et al., 2011, 2014) because thermal fatigue as the formation of Itokawa particles could not be excluded.

As we focused on the investigation of the axial ratios of many fragments in this study, we did not investigate the interior (e.g., cracks and pores) of the fragments, which would require a higher imaging resolution. A quantitative investigation for the interior of impact fragments would be needed in the future, to compare the interior of Itokawa particles.

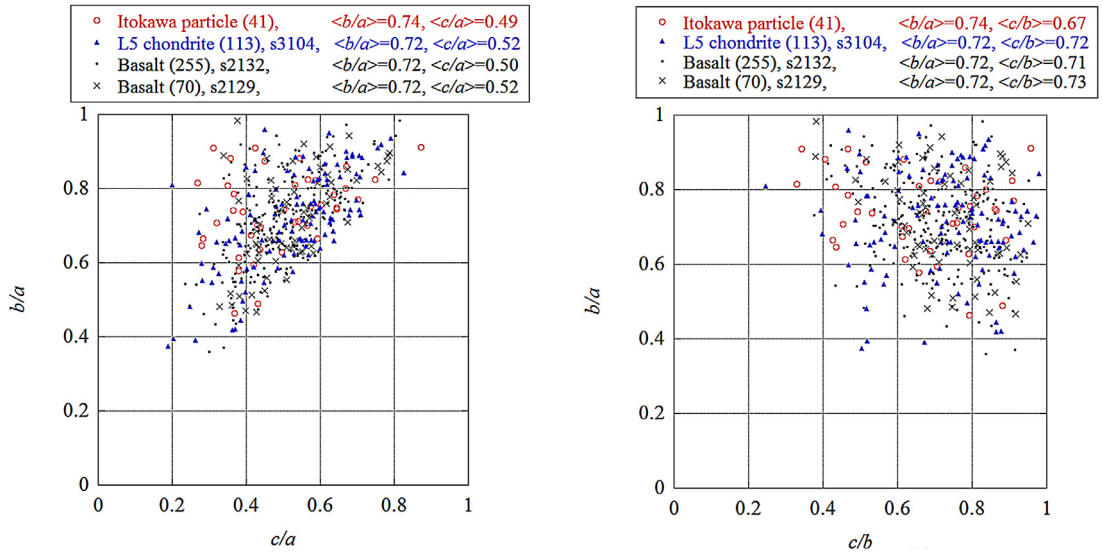

Fig. 7. Diagrams for the shape distributions of Itokawa regolith particles investigated by Tsuchiyama et al. (2014) and S-sized fragments from L5 chondrite (s3104) and basalts (s2132, s2129). Here, the shape of Itokawa particles was determined using the *BU* method instead of *EA* method (see Appendix A) for comparison. The number of the fragments in each size group is given in parentheses and, mean *b/a, c/a* and *c/b* are indicated in square brackets. We excluded 7 particles confirmed to be pieces of original particles fragmented during curation, as indicated by the branch number in Tsuchiyama et al. (2014).

5.3. Comparison with lunar regolith particles

Lunar regolith particles are also strongly influenced by impact phenomena, which is why their shapes must reflect their histories on the lunar surface. From the results of our present experiments, we expect the shapes of M- and S-sized lunar regolith particles to be similar to those of Itokawa regolith particles and the experiment impact fragments. However, their shapes are more spherical (or equant) according to recent studies (e.g., Tsuchiyama et al., 2011; Katagiri et al., 2014). For instance, Katagiri et al. (2014) have examined the three-dimensional microstructure of 74 lunar regolith particles from Apollo 16 with sizes from 105 to 205 μm using synchrotron radiation (SR)-based microtomography at SPring-8. The results show that the mean axial ratios of *b/a, c/a* and *b/a* (*EA* method) are 0.79, 0.59 and 0.77, respectively.

In their two-dimensional analysis, for instance, Liu et al. (2008) investigated numerous regolith particles (1200–7200 particles for each sample) in five Apollo lunar soils. The distributions of aspect ratios of all five lunar samples show a peak at ~0.7. This means that the aspect ratios of lunar regolith particles are compatible with the values of our experiments, assuming that the aspect ratio corresponds to *b/a* in the experiments (The *c* axis of the particles would become roughly perpendicular to the surface of the detector stand). Unfortunately though, the error of these data is considered to be large because the direction of the *c* axis would be slightly inclined during the measurement. Therefore, it is difficult to confirm from their study that the lunar regolith particles are more spherical.

In a more recent study however, Tsuchiyama et al. (2017) proposed that the three-dimensional shapes of lunar regolith particles (>1000 particles) are more spherical compared with Itokawa regolith particles. Abrasion during movement may affect the shapes of the former because their average residence period on the surface is much longer than that of asteroid regolith particles.

6. Conclusions

We have primarily investigated the shapes of fine fragments smaller than 120 μm (S-sized fragments) created in impacts in the range from cratering to catastrophic disruption ($Q = 230–8540$ J/kg in basalt targets; $Q = 1930$ and 13,540 J/kg in L5 chondrite targets) using synchrotron radiation-based microtomography at SPring-8. The shape distributions of S-sized fragments of basaltic and L5 chondrite targets are similar, distributed around the mean values of the axial ratio $2:\sqrt{2}:1$. The shape distributions of these small fragments are independent of *Q* which means that the degree of target fragmentation does not affect their shapes.

The shapes of L-sized fragments on the other hand are influenced by the degree of fragmentation as already pointed by Michikami et al. (2016), i.e. the mean *c/a* ratios decrease as the specific energy, *Q*, decrease. Therefore, the shapes of L-sized fragments differ from S-sized fragments which are considered to be produced by the different mechanism compared with L-sized fragments, namely by multiple rarefaction waves in the target.

In order to investigate the relationship between the petrographic textures and the shapes of S-sized fragments, we classified the S-sized basalt fragments into three types (Type P, P/G and G). The result shows that the shape distributions of three types are similar, distributed around mean values of the axial ratios *b/a* ~0.7 and *c/a* ~0.5. Hence, we concluded from our impact experiments that the petrographic textures and the crystal grain boundaries do not significantly affect the shapes of S-sized fragments by impacts. On the other hand, in thermal fatigue caused by the day-night temperature cycles on an asteroid surface, the petrographic textures and the crystal grain boundaries would affect the shapes of the fragments (Molaro et al., 2015). As the shape distribution of the Itokawa particles is similar to those of S-sized fragments from impacts, we therefore conclude that the Itokawa particles have not been produced by thermal fatigue and are likely to be impact fragments on the asteroid surface.

Acknowledgments

The authors acknowledge Dr. T. Kadono of University of Occupational and Environmental Health for useful comments. We also thank Dr. M. Yamanouchi and Dr. A. M. Nakamura for the support of the compressive wave velocity. The experiments described in this paper were conducted and supported by ISAS/JAXA in collaboration with the Hypervelocity Impact Facility (former facility name: the Space Plasma Laboratory). Dr. M. Nakamura and Dr. S. Okumura of Tohoku University helped us to make plaster models of Itokawa particles using a 3D printer. We also thank Professor

Table A.1
Mean axial ratios of *b/a*, *c/a* and *c/b* for 41 Itokawa particles by Tsuchiyama et al. (2014) obtained from different measurement method (see text). The data of "*EA*, *TD* and *BU*" were acquired from CT images. The data of "*BU* with a caliper" were measured with a caliper.

Method	*b/a*	*c/a*	*c/b*
EA	0.71	0.45	0.63
TD	0.80	0.53	0.67
BU	0.74	0.49	0.67
BU with a caliper	0.75	0.49	0.66

M. Zolensky and an anonymous referee for their careful review of the manuscript and their constructive comments. This study was partly supported by the JSPS (KAKENHI No. 15H05695 for AT). AH would like to acknowledge financial support by STFC under grant no. ST/P000657/1.

Appendix A. Differences arising from different measurement methods

In previous experiments, the fragment shapes were usually defined in term of the axial ratios of *b/a* and *c/a*, where *a, b* and *c* are defined as the dimensions of a fragment along three orthogonal axes. However, the definitions of the fragment shapes are not unique. Thus, in order to compare our experiments with previous experiments, the resulting differences in the measurement methods warrant some attention.

The definitions of the fragment shapes can be classified into the following categories. The first definition approximates the fragment shape as an ellipsoid, and then *a, b* and *c* are measured as the dimensions of a fragment along three orthogonal axes. Note that the order of the measurements with regard to the *a, b* and *c* axes does not affect the result. This method was used by Tsuchiyama et al. (2011, 2014), Katagiri et al. (2014) and Durda et al. (2015). We will call this method *EA* (*ellipsoidal approximation*) method here. The second and third categories do not assume that the fragment shape is ellipsoidal. Instead, a fragment is defined as a parallelepiped of a bounding box. The three sides of the box are measured as the three axes of *a, b* and *c*. There are two methods, depending on which fragment dimension is measured first. These are called *top-down* and *bottom-up* methods by La Spina and Paolicchi (1996). In the case of the *top-down* method (*TD* method from now on), the longest dimension of the fragment is measured first, then the longest dimension perpendicular to this, and finally the longest dimension perpendicular to both. This method was used by Capaccioni et al. (1984, 1986) and Giblin et al. (1994). For the *bottom-up* method (*BU* method from now on), the above measurement order is reversed. This method was used by Fujiwara et al. (1978) and Michikami et al. (2016). In our study, we used the *BU* method, as mentioned above.

According to La Spina and Paolicchi (1996), the differences arising from various methods are less severe, albeit not negligible. To confirm this, we investigated the differences using the data of Itokawa particles (Table A.1). The axial ratios of Itokawa particles have already been measured using the *EA* method and were presented by Tsuchiyama et al. (2011, 2014), revealing their three-dimensional (3D) structure and other properties using X-ray microtomography. In the case of the *EA* method, the mean *b/a* and *c/a* ratios in these Itokawa particles (41 in total) are 0.71 and 0.45, respectively. Deriving the mean *b/a* and *c/a* ratios using the *TD* and *BU* methods results in slightly larger values than using the *EA* method. The differences arising from these measurement methods are not negligible, and are roughly within ±0.04. Further investigation for the different methods would be necessary.

In addition to these differences, we have also investigated the differences arising from computational calculation and manual measurement in the *BU* method using the same data of Itokawa particles. This is because the values of the axial ratios measured with a caliper (manual measurement) in previous experiments may include a slight error. To confirm this, we made exactly-enlarged plaster models of Itokawa particles using a 3D printer, based on detailed three-dimensional structure data obtained from microtomography (the manufacture error can be ignored in the precision of this inspection), and then the shapes of the models were measured with a caliper by the same two individuals who measured the shapes of fragments larger than 4 mm in Michikami et al. (2016). The differences arising from computational calculation and manual measurement are significantly small, the difference in the mean axial ratios being less than 1×10^{-2}. Therefore, we are confident that the axial ratios of fragments in this experiment and previous values used by Michikami et al. (2016) are highly reliable.

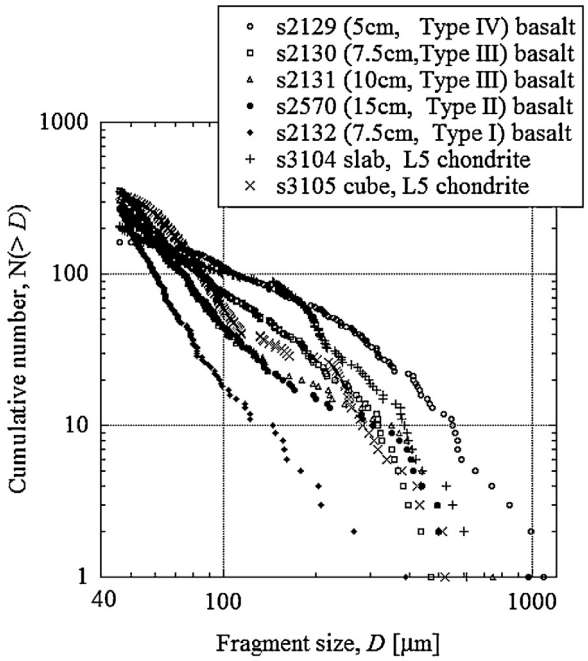

Fig. B.1. Size distributions of M- and S-sized fragments shown in Fig. 3 of basalts (s2129, s2130, s2131, s2132 and s2570) and Fig. 6 of L5 chondrites (s3104 and s3105). Horizontal and vertical axes show the size of the fragments and the cumulative number of the fragments with a size greater than *D*, respectively, where *D* is the sphere-equivalent diameter derived from the particle volume.

Appendix B. Size distributions of M- and S-sized fragments

Fig. B.1 gives the size distributions of M- and S-sized fragments shown in Fig. 3 for basalts (s2129, s2130, s2131, s2132 and s2570) and Fig. 6 for L5 chondrites (s3104 and s3105). In this study, we focused on the collection of fine fragments smaller than 200 μm in order to compare these with Itokawa particles. Thus, because we only arbitrarily selected a part of fine fragments, their size distributions may not be reflective of the real size distributions in the size ranges from 40 μm to 4 mm.

References

Aström, J.A., 2006. Statistical models of brittle fragmentation. Adv. Phys. 55, 247–278.
Bianchi, R., et al., 1984. Experimental simulation of asteroidal fragmentation by macroscopic hypervelocity impacts against free falling bodies. Astron. Astrophys. 139, 1–6.
Capaccioni, F., et al., 1984. Shapes of asteroids compared with fragments from hypervelocity impact experiments. Nature 308, 832–834.
Capaccioni, F., et al., 1986. Asteroidal catastrophic collisions simulated by hypervelocity impact experiments. Icarus 66, 487–514.

Durda, D.D., et al., 2015. The shapes of fragments from catastrophic disruption events: effects of target shape and impact speed. Planet. Space Sci. 107, 77–83.
Flynn, G.J., Durda, D.D., 2004. Chemical and mineralogical size segregation in the impact disruption of inhomogeneous, anhydrous meteorites. Planet. Space Sci. 52, 1129–1140.
Fujiwara, A., Kamimoto, G., Tsukamoto, A., 1978. Expected shape distribution of asteroids obtained from laboratory impact experiments. Nature 272, 602–603.
Fujiwara, A., 1980. On the mechanism of catastrophic destruction of minor planets by high-velocity impact. Icarus 41, 356–364.
Giblin, I., et al., 1994. Field fragmentation of macroscopic targets simulating asteroidal catastrophic collisions. Icarus 110, 203–224.
Harries, D., et al., 2016. Secondary submicrometer impact cratering on the surface of asteroid 25143 Itokawa. Earth Planet. Sci. Lett. 450, 337–345.
Holsapple, K., et al., 2002. Asteroid impacts: laboratory experiments and scaling laws. In: Bottke, W.F., Cellino, A., Paolicchi, P., Binzel, R.P. (Eds.), Asteroids III. University of Arizona Press, Tucson, pp. 443–462.
Kadono, T., Arakawa, M., 2002. Crack propagation in thin glass plate caused by high velocity impact. Phys. Rev. E65, 035107.
Katagiri, J., et al., 2014. Investigation of 3D grain shape characteristics of lunar soil retrieved in Apollo 16 using image-based discrete-element modeling. J. Aerosp. Eng. ASCE 28 (4), 04014092.
La Spina, A., Paolicchi, P., 1996. Catastrophic fragmentation as a stochastic process: sizes and shapes of fragments. Planet. Space Sci. 44, 1563–1578.
Liu, Y., et al., 2008. Characterization of lunar dust for toxicological studies. II: texture and shape characteristics. J. Aerosp. Eng. 21 (4), 272–279.
Matsui, T., et al., 1982. Laboratory simulation of planetesimal collision. J. Geophys. Res. 87, 10968–10982.
Matsui, T., Waza, T., Kani, K., 1984. Destruction of rocks by low velocity impact and its implications for accretion and fragmentation processes of planetesimals. J. Geophys. Res. Suppl. 89, B700–B706.
Matsumoto, T., et al., 2016. Nanomorphology of Itokawa regolith particles: application to space-weathering processes affecting the Itokawa asteroid. Geochim. Cosmochim. Acta 187, 195–217.
Meakin, P., 1984. Diffusion-controlled deposition on surfaces: cluster-size distribution, interface exponents, and other properties. Phys. Rev. B 30, 4207–4214.
Medvedev, R.V., Gorbatsevich, F.I., Zotkin, I.T., 1985. Determination of the physical properties of stony meteorites with application to the study of processes of their destruction. Meteoritika 44, 105–110 (in Russian).
Michikami, T., et al., 2016. Fragment shapes in impact experiments ranging from cratering to catastrophic disruption. Icarus 264, 316–330.
Molaro, L.J., Byrne, S., Langer, A.S., 2015. Grain-scale thermoelastic stresses and spatiotemporal temperature gradients on airless bodies, implications for rock breakdown. J. Geophys. Res. Planets 120, 255–277.
Nakamura, T., et al., 2011. Itokawa dust particles: a direct link between S-type asteroids and ordinary chondrites. Science 333, 1113–1116.
Nakano, T., et al., 2000. Observation and analysis of internal structure of rock using X-ray CT. J. Geol. Soc. Jpn. 106, 363–378.
Nakano, T., et al., 2006. "Slice-Softwares for Basic 3-D Analysis" (Web). Japan Synchrotron Radiation Research Institute http://www-bl20.spring8.or.jp/slice/.
Nelson, V.E., Rubin, A.E., 2002. Size-frequency distributions of chondrules and chondrule fragments in LL3 chondrites: implications for parent-body fragmentation of chondrules. Meteorit. Planet. Sci. 37, 1361–1376.
Takagi, Y., Mizutani, H., Kawakami, S., 1984. Impact fragmentation experiments of basalts and pyrophyllites. Icarus 59, 462–477.
Tsuchiyama, A., et al., 2005. Quantitative evaluation of attenuation contrast of X-ray computed tomography images using monochromatized beams. Am. Mineral. 90, 132–142.
Tsuchiyama, A., et al., 2011. Three-dimensional structure of Hayabusa samples: origin and evolution of Itokawa regolith. Science 333, 1125–1128.
Tsuchiyama, A., et al., 2014. Three-dimensional microstructure of samples recovered from asteroid 25143 Itokawa: comparison with LL5 and LL6 chondrite particles. Meteorit. Planet. Sci. 49, 172–187.
Tsuchiyama, A. et al., 2017. Shape evolution of regolith particles on airless bodies; comparison with returned samples and impact and abrasion experiments. Abstract in JpGU, PPS03-13.
Uesugi, K., et al., 2012. Development of fast and high throughput tomography using CMOS image detector at SPring-8. Proc. SPIE 8506, 85060I.
Yomogida, K., Matsui, T., 1983. Physical properties of ordinary chondrites. J. Geophys. Res. 88, 9513–9533.
Yurimoto, H., et al., 2011. Oxygen isotopic compositions of asteroidal materials returned from Itokawa by the Hayabusa mission. Science 333, 1116–1119.